CrossMark

Modeling the effects of extracellular potassium on bursting properties in pre-Bötzinger complex neurons

Bartholomew J. Bacak[1] ⓘ · **Joshua Segaran**[2] · **Yaroslav I. Molkov**[3]

Abstract There are many types of neurons that intrinsically generate rhythmic bursting activity, even when isolated, and these neurons underlie several specific motor behaviors. Rhythmic neurons that drive the inspiratory phase of respiration are located in the medullary pre-Bötzinger Complex (pre-BötC). However, it is not known if their rhythmic bursting is the result of intrinsic mechanisms or synaptic interactions. In many cases, for bursting to occur, the excitability of these neurons needs to be elevated. This excitation is provided *in vitro* (e.g. in slices), by increasing extracellular potassium concentration (K_{out}) well beyond physiologic levels. Elevated K_{out} shifts the reversal potentials for all potassium currents including the potassium component of leakage to higher values. However, how an increase in K_{out}, and the resultant changes in potassium currents, induce bursting activity, have yet to be established. Moreover, it is not known if the endogenous bursting induced *in vitro* is representative of neural behavior *in vivo*. Our modeling study examines the interplay between K_{out}, excitability, and selected currents, as they relate to endogenous rhythmic bursting. Starting with a Hodgkin-Huxley formalization of a pre-BötC neuron, a potassium ion component was incorporated into the leakage current, and model behaviors were investigated at varying concentrations of K_{out}. Our simulations show that endogenous bursting activity, evoked *in vitro* by elevation of K_{out}, is the result of a specific relationship between the leakage and voltage-dependent, delayed rectifier potassium currents, which may not be observed at physiological levels of extracellular potassium.

1 Introduction

Nervous systems of invertebrates and vertebrates contain neuronal structures capable of generating rhythmic neuronal activity, even without external input, i.e. endogenous rhythmicity, that controls several motor behaviors, such as locomotion and respiration. One such rhythmic structure, the medullary pre-Bötzinger complex (pre-BötC), represents the putative site for inspiratory rhythm generation in mammals (Smith et al. 1991, 2013; Johnson et al. 1994). Recordings from the medulla, performed *in vivo*, show a rhythmic activity pattern that projects to pre-motor and motorneurons that cause the cyclical contraction and relaxation of various respiratory muscles (Ramirez et al. 2002; Richter and Spyer 2001; Smith et al. 2000). This rhythm was further characterized as a "three-phase" pattern, containing inspiratory, post-inspiratory, and augmenting-expiratory phases (Lawson et al. 1989; Richter 1982, see Richter and Smith 2014 for review). Analogous activity patterns have been extensively characterized *in vitro*. When progressive caudal transections are made, the normal three-phase pattern switches to a two-phase rhythm (inspiration and expiration), and finally to a single, only inspiratory,

Action Editor: Bard Ermentrout

✉ Bartholomew J. Bacak
bjb87@drexel.edu

[1] Department of Neurobiology and Anatomy, Drexel University College of Medicine, Room 274, 2900 W. Queen Ln., Philadelphia, PA 19129, USA

[2] Massachusetts Institute of Technology, Cambridge, MA, USA

[3] Department of Mathematics & Statistics, Georgia State University, Atlanta, GA, USA

⚛ Springer

phase (Rybak et al. 2007; Smith et al. 2007, 2009). The one-phase rhythm occurred when only the pre-BötC remained intact, and thus indicates that a network of pre-BötC neurons is capable of endogenous bursting. Moreover, it has been demonstrated that some pre-BötC neurons continued generating rhythmic bursting, in these *in vitro* preparations, even after synaptic connections were blocked (Johnson et al. 1994; Thoby-Brisson and Ramirez 2001).

A successive transition from quiescence, to bursting, and then to tonic spiking can be induced, *in vitro*, in an individual neuron, by progressively increasing the resting membrane potential. This can be performed directly, by electrical current (Koshiya and Smith 1999), or by elevation of extracellular potassium concentration, K_{out}, from its physiological level of 3–4 mM up to 8–9 mM (Johnson et al. 1994; Shao and Feldman 1997; Del Negro et al. 2001; Thoby-Brisson and Ramirez 2001). Del Negro et al. 2001 showed that further elevation of K_{out} caused a transition from bursting to tonic spiking. It was proposed that this elevation of K_{out} was necessary to increase neuronal excitability (neuronal membrane depolarization) and compensate for a lack of external excitatory drives operating in the more intact *in vivo* systems. Despite the extensive study of endogenously bursting neurons of the pre-BötC, *in vitro*, it has yet to be determined, due to experimental limitations, if endogenous bursting occurs physiologically.

To address these limitations, several computational models have been developed to study the mechanisms underlying bursting behaviors in pre-BötC neurons. Butera et al. 1999a, b suggested that the rhythmic bursting observed in pre-BötC slice preparations may arise from a persistent (or slowly inactivating) sodium current (I_{NaP}). The presence of I_{NaP} in pre-BötC neurons was then confirmed (Del Negro et al. 2001; Rybak et al. 2003a; Koizumi and Smith 2008), and pre-BötC rhythmic activity in medullary slices could be abolished by the I_{NaP} blocker, riluzole (Rybak et al. 2004a; Koizumi and Smith 2008). Large scale models of the broader respiratory network, also using the I_{NaP}-dependent burst mechanism, have reproduced a breadth of experimental findings, including the transitions described in the first paragraph (Molkov et al. 2010; Rybak et al. 2004b, c, 2007). In these models, elevation of K_{out} and its effects on neurons were not explicitly simulated. Instead, neuronal excitability was directly adjusted by modulating the leakage reversal potential, E_L, leading to membrane depolarization. However, elevation of K_{out} does not only affect E_L, but also the potassium reversal potential, E_K, and therefore all potassium currents. The delayed rectifier potassium current, I_K, is of particular interest because of its role in neuronal after spike repolarization (Rybak et al. 2003b). Higher E_K values weaken I_K, which in turn can affect regimes of neuronal activity and transitions between regular spiking and bursting.

The primary aim of this study was to evaluate the plausibility of specific neuronal bursting mechanisms at a range of

K_{out} values that encompasses those observed *in vivo* and the elevated concentrations used for *in vitro* experiments. We developed a novel model formalization where both I_K and I_L were dependent on K_{out}. The results of our study suggest that the mechanisms thought to underlie endogenous bursting *in vitro*, e.g. the persistent-sodium current in our model, were insufficient to produce this behavior when K_{out} was reduced to *in vivo* concentrations.

2 Methods

2.1 Model description

Our model of a single pre-BötC neuron represents an extension of previous conductance-based models (Butera et al. 1999a, b; Rybak et al. 2004a). The model includes the following currents: fast sodium (I_{Na}), persistent (slowly inactivating) sodium (I_{NaP}), delayed rectifier potassium, (I_K) leakage (I_L), and synaptic (I_{Syn}) currents.

The neuron's membrane potential (V) is defined using the differential equation:

$$C \cdot \frac{dV}{dt} = -I_{Na} - I_{NaP} - I_K - I_L - I_{Syn}, \quad (1)$$

where C is the membrane capacitance.

The currents are modeled by the following equations:

$$I_{Na} = \overline{g}_{Na} \cdot m_{Na}^3 \cdot h_{Na} \cdot (V - E_{Na}); \quad (2)$$

$$I_{NaP} = \overline{g}_{NaP} \cdot m_{NaP} \cdot h_{NaP} \cdot (V - E_{Na}); \quad (3)$$

$$I_K = \overline{g}_K \cdot n^4 \cdot (V - E_K); \quad (4)$$

$$I_L = g_L \cdot (V - E_L); \quad (5)$$

$$I_{Syn} = g_{Syn} \cdot (V - E_{Syn}), \quad (6)$$

where: $\overline{g}_{Na}$, $\overline{g}_{NaP}$, and $\overline{g}_K$ are maximal conductances for the fast sodium, persistent sodium, and potassium delayed rectifier currents, respectively; g_L and g_{Syn} are the leakage and synaptic conductances, respectively; m_{cur} and h_{cur} (where the index, *cur*, identifies either *Na* or *NaP*) represent the activation and inactivation gating variables for the corresponding voltage-gated sodium channels whose dynamics are described by the following equations:

$$\tau_{h,cur}(V) \cdot \frac{dh_{cur}}{dt} = h_{\infty,cur}(V) - h_{cur}; \quad (7)$$

$$\tau_{m,cur}(V) \cdot \frac{dm_{cur}}{dt} = m_{\infty,cur}(V) - m_{cur}, \quad (8)$$

where the voltage dependent inactivation, $h_{\infty,cur}$, and the voltage dependent activation, $m_{\infty,cur}$, have voltage dependent time constants, $\tau_{h,cur}$ and $\tau_{m,cur}$, respectively. These voltage

dependent gating functions for the sodium currents, I_{NaP} and I_{Na}, are governed by the following equations, first described by Butera et al. 1999a:

$$h_{\infty,cur}(V) = \left(1 + exp\{(V-V_{h,cur})/k_{h,cur}\}\right)^{-1}; \qquad (9)$$

$$m_{\infty,cur}(V) = \left(1 + exp\{(V-V_{m,cur})/k_{m,cur}\}\right)^{-1}; \qquad (10)$$

$$\tau_{h,cur}(V) = \tau_{h,cur,max}/cosh\{(V-V_{h,\tau,cur})/k_{h,\tau,cur}\}; \qquad (11)$$

$$\tau_{m,cur}(V) = \tau_{m,cur,max}/cosh\{(V-V_{m,\tau,cur})/k_{m,\tau,cur}\}. \qquad (12)$$

The parameters of Eqs. (9–12) may be found in Section 2.2. The voltage dependent activation, n, of the delayed rectifier potassium current, I_K, follows the same general form as the other currents activations:

$$\tau_n(V) \cdot \frac{dn}{dt} = n_\infty(V) - n, \qquad (13)$$

and obeys the voltage dependent functions described by Huguenard and McCormick 1992:

$$n_\infty(V) = k_1(V)/(k_1(V) + k_2(V)); \qquad (14)$$

$$\tau_n(V) = (k_1(V) + k_2(V))^{-1}; \qquad (15)$$

$$k_1(V) = n_A \cdot (n_{AV} + V)/(1-exp\{-(n_{AV} + V)/n_{Ak}\}); \qquad (16)$$

$$k_2(V) = n_B \cdot exp\{-(V + n_{BV})/n_{Bk}\}. \qquad (17)$$

All parameters for Eqs. (13–17) are listed in Section 2.2.

The reversal potentials, E_{Na} and E_K in Eqs. (2–4), for Na^+ and K^+ ions, were calculated with the Nernst equation:

$$E_{ion} = \frac{R \cdot T}{n \cdot F} \cdot ln \frac{Ion_{out}}{Ion_{in}}, \qquad (18)$$

where R is the universal gas constant, T is the temperature in Kelvin, n is the charge of the ion, and F is Faraday's constant.

In order to explore the mechanisms behind the K^+-dependent neuronal excitability a detailed description of the leakage current (I_L) was developed. The K^+ and Cl^- components of the leak current hyperpolarize the cell, while the Na^+ component causes neuronal depolarization (Forsythe and Redman 1988). Each of these ions has a conductance (g_x) and a reversal potential (E_x), that were incorporated into I_L as follows:

$$g_L \cdot (V-E_L) = g_{LK} \cdot (V-E_K) + g_{LNa} \cdot (V-E_{Na})$$
$$+ g_{LCl} \cdot (V-E_{Cl}); \qquad (19)$$

$$g_L = g_{LK} + g_{LCl} + g_{LNa}; \qquad (20)$$

$$E_L \cdot g_L = E_K \cdot g_{LK} + E_{Cl} \cdot g_{LCl} + E_{Na} \cdot g_{LNa}, \qquad (21)$$

where E_L is the effective reversal potential of the leakage current and g_L is its conductance (both are assumed to be known). Equation (19) is a general equation showing that I_L is the sum of the three distinct currents. Equations (20) and (21) are derived from (19). We included the Cl ion because it is associated with a hyperpolarizing current, as it brings negative charge into the cell, and it has been proven to be part of the leakage current in previous experimental studies (Forsythe and Redman 1988). Only the potassium component of the leak current is affected by variations in extra cellular potassium concentration. A dimensionless parameter, δ, was introduced to specify the ratio of potassium contribution to the hyperpolarizing ionic component of I_L, of K^+ and Cl^-:

$$\delta \cdot (g_{LCl} + g_{LK}) = g_{LK}, \qquad (22)$$

Increasing δ increases g_{LK}, thus changing K_{out} has a larger effect on I_L. By solving the linear system (20), (21), (22), we calculated the conductances of each ionic component's contribution to the overall leakage current, under standard conditions with K_{out} of 4 mM, e.g. g_{LK} is defined by the formula:

$$g_{LK} = \frac{\delta \cdot (E_L - E_{Na}) \cdot g_L}{\delta \cdot (E_K - E_{Cl}) - (E_{Na} - E_{Cl})}, \qquad (23)$$

where $E_L = -64$ mV, $E_{Cl} = -90$ mV, and $g_L = 2.5$ nS are constants taken from Jasinski et al. 2013, and E_{Na} was calculated using standard intracellular and extracellular Na^+ concentrations (see section 2.2 Model Parameters). The conductances of individual ions in I_L were calculated using Eq. (23) with a K_{out} of 4 mM and a varying value of δ.

We refer to the excitatory synaptic conductance (g_{syn}) mimicking network input for the synaptic current, I_{syn}, as *drive*. This parameter was varied to induce different neuronal regimes in the system. E_{syn} is the reversal potential of excitatory synaptic current given in the following section.

2.2 Model parameters

The following default values of parameters were used, except where it is indicated in the text that some parameter values were varied in particular simulations:

Membrane capacitance (pF): $C = 36$.
Universal gas constant (J/(mol·K)): $R = 8.314$.
Faraday constant (C/mol): $F = 9.648 \cdot 10^4$.
Temperature (K): $T = 308$.
Maximal conductances (nS): $\overline{g}_{Na} = 120$, $\overline{g}_{NaP} = 5$, $\overline{g}_K$ is varied, $g_L = 2.5$, $g_{syn} = 0$.
Reversal potentials (mV): $E_{Na} = \frac{R \cdot T}{F} ln \frac{Na_{out}}{Na_{in}}$, $E_K = \frac{R \cdot T}{F} ln \frac{K_{out}}{K_{in}}$, $E_L = -64$, $E_{Cl} = -90$, $E_{syn} = -10$.
Ionic concentrations (mM): $Na_{out} = 120$, $Na_{in} = 15$, $K_{out} = $ varied, $K_{in} = 140$.
Parameters for I_{Na}, I_{NaP} and I_K: $V_{m,Na} = -43.8$ mV, $k_{m,Na} = 6$, $k_{m,\tau,Na} = 14$, $V_{h,Na} = -67.5$ mV, $k_{h,Na} = -10.8$, $k_{h,\tau,Na} = -12.8$, $V_{m,NaP} = -47.1$ mV, $k_{m,NaP} = 3.1$, $k_{m,\tau,}$

$_{NaP} = 6.2$, $V_{h,NaP} = -60$ mV, $k_{h,NaP} = 9$, $k_{h,\tau,NaP} = 9$, $n_A = 0.01$, $n_{AV} = 44$, $n_{Ak} = 5$, $n_B = 0.17$, $n_{BV} = 49$, $n_{Bk} = 40$. Time constants (ms): $\tau_{m,Na,max} = 0.25$, $\tau_{h,Na,max} = 8.46$, $\tau_{m,NaP,max} = 1$, $\tau_{h,NaP,max} = 5000$.

2.3 Classification of neuronal behaviors with bifurcation diagrams

The model produced a variety of qualitatively unique behaviors including: quiescence (silence), bursting (Figs. 1a, c), tonic spiking (Fig. 1b), and sustained depolarization (Fig. 1d). Bursting behaviors were separated into two groups: regular bursts (see Fig. 1a) and plateau-like bursts with a transient depolarization block (maintained depolarization) within a cluster of spikes (see Fig. 1c), and will heretofore be referred to as "regular" and "depolarization block" (DB) bursts, respectively. Bursting with a depolarization block (DB bursting) is typically dismissed as an artifact or transitional regime in experimental recordings, see Thoby-Brisson and Ramirez 2001 for an example of this bursting behavior. One-dimensional bifurcation diagrams were constructed (see below) to detect and classify bursting behaviors. Bifurcation diagrams were also used for the analysis of the dramatic changes in the system's behavior when *drive*, K_{out}, and δ were varied.

We used a technique involving the construction of Poincaré sections to create bifurcation diagrams (Kantz and Schreiber 2004). The Poincaré section was constructed by locating instances of the neuron's potential crossing a chosen threshold, −35 mV, in a specified direction. The time between these instances, i.e. the interspike interval, was plotted against specific bifurcation parameters, e.g. K_{out}, *drive*, or δ (c.f. Fig. 2a–c). Such bifurcation diagrams show qualitative changes in the system's behavior as the parameters were varied.

Two-dimensional bifurcation diagrams have different bifurcation parameters on the *x*- and *y*-axis and the regions of bursting are shaded black (see Fig. 2d). Occasionally

bistabilities occurred when two unique regimes co-existed at the same value of bifurcation parameters (see Fig. 2c at *drive* [0.3, 0.34] for a representative example). To find bistabilities, the simulation was performed with a slowly increasing *drive* and then repeated with slowly decreasing *drive*. The time interval separating changes in *drive* was sufficiently large to allow the system to closely converge to its steady state prior to the calculation of interspike intervals. Similar observations have been made with *in vitro* preparations that demonstrate switching between quiescence and bursting behavior when a small transient current pulse is applied (Guttman et al. 1980). The in silico parallel creates two stable regions of attraction and applying an external *drive* can perturb the system away from one region and towards the other (Rinzel 1985). Transitions are also completed using external *drive* in regions where no bistability exists; progressively increasing an external *drive* will cause transitions from silence to bursting and from bursting to tonic spiking for certain fixed parameter values.

2.4 Qualitative analysis

Fast-slow decomposition analysis of the system involved the projection of the system's dynamics onto the plane of variables describing membrane potential, V, and the inactivation of persistent sodium, h_{NaP}. The time constants for V, h_{Na}, m_{Na}, m_{NaP}, n, and h_{NaP} are such that the slower variable, h_{NaP}, may be treated as a fixed parameter of the five-dimensional fast subsystem with dynamical variables: V, h_{Na}, m_{Na}, m_{NaP}, and n. The equilibrium solutions, or critical points, of the fast subsystem were projected into (h_{NaP}, V) and formed the slow-manifold as h_{NaP} was varied, see Fig. 3a blue curve. The slow-manifold had a cubic shape with three branches. The lower and middle branches are connected by a point which is the lower knee (LK) of the slow-manifold. From right to left, along the slow-manifold, critical points become unstable at a Hopf bifurcation
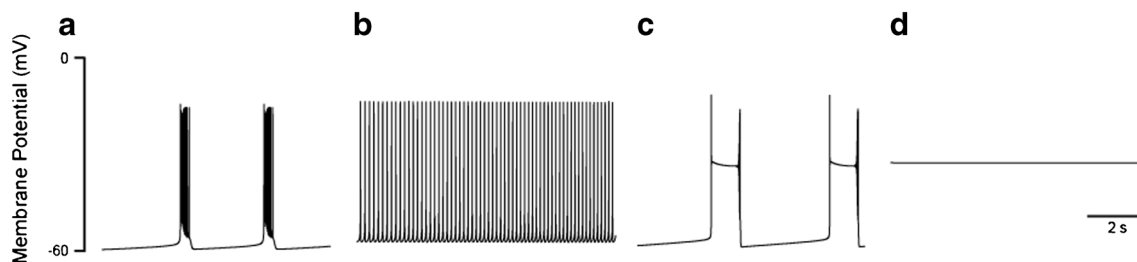

Fig. 1 Neuronal voltage patterns. **a** Bursting occurs when groups of multiple action potentials are followed by a period of silence. **b** Tonic (spiking) occurs when individual action potentials occur repeatedly, without a period of silence. **c** DB bursting has periods of silence separating bursts that contain a period of tonic depolarization. **d**

Depolarization block is defined as a steady state characterized by a high membrane potential (about −35 mV), as a result of a weak delayed rectifier potassium current, I_K (discussed in text) which renders a neuron unable to spike
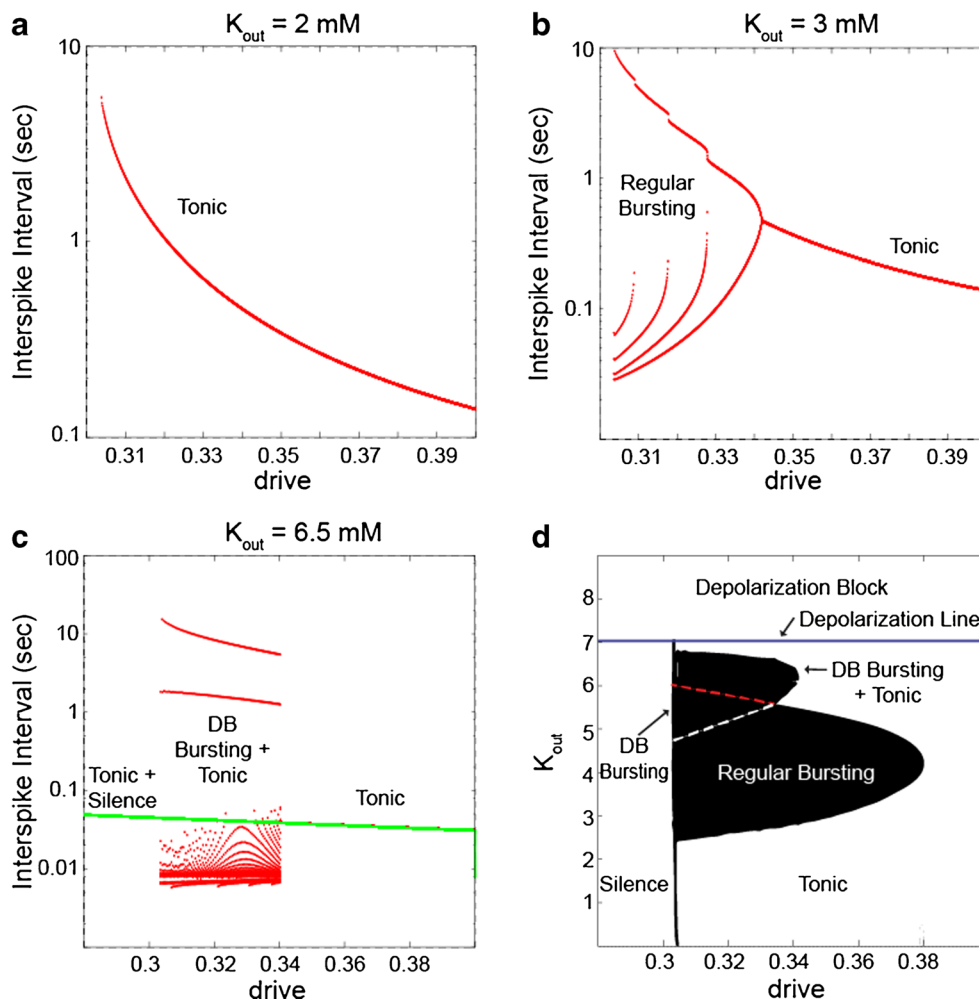
Fig. 2 Bifurcation diagrams with $\delta = 0$. **a**–**c**. Interspike interval was calculated as *drive* was increased (*red dots*) and decreased (*green dots*). **a** One-dimensional bifurcation diagram with $K_{out} = 2.0$ mM. Tonic spiking occurred when *drive* > 0.3 and silence was observed at lower *drive*. **b** One-dimensional bifurcation diagram with $K_{out} = 3.0$ mM. At this lower concentration of K_{out}, regular bursting occurred for *drive* values between 0.303 and 0.34. Regular bursting has only one intraburst interval greater than one second, as opposed to the two branches characteristic of DB bursting. As before, tonic activity occurred at higher levels of *drive*. **c** One-dimensional bifurcation diagram with interspike interval versus *drive* at K_{out} of 6.5 mM. A bistability of silence and tonic spiking occurred when *drive* < 0.3. When *drive* is slightly greater than 0.3, a transition from silence to DB bursting occurred. DB bursting is characterized by the existence of two

branches that correspond to interspike interval durations greater than one second. When *drive* was between 0.3 and 0.35, DB bursting coexisted with tonic spiking. At higher levels of *drive*, only tonic spiking occurred. **d** Two-dimensional bifurcation diagram, showing neuronal regimes as K_{out} and *drive* vary, while δ was fixed at 0. Both DB and regular bursting regimes are *shaded black*. The boundary between silent and active regimes, i.e. the activation curve, was vertical. The portion of bursting above the dashed white line represents areas of DB bursting, and the areas below represent regular bursting. *The dashed red line* separates DB bursting (*below line*) from a region of bistability between DB bursting and tonic spiking. Boundaries separating qualitative behaviors were calculated using one-dimensional bifurcation diagrams that varied K_{out} when *drive* was fixed

point (HB, blue circle), with periodic orbits emerging (red lines represent the extrema of the voltage on the emerging periodic orbit). The h_{NaP}-nullcline, calculated when the first derivative of $h_{NaP} = 0$, see Eq. (7), is represented by a black dashed line, and the solution to the full system is depicted by a trajectory drawn with a solid black line.

Fast-slow decomposition methods reveal the mechanisms underpinning the regular and DB bursts. These regimes each have the same general structure, i.e. that

of a saddle-loop (homoclinic) bifurcation in the fast subsystem responsible for the burst termination (explained later in more detail), and differ primarily in the positioning of the LK, HB, and the h_{NaP}-nullcline. When at rest, the system's trajectory travels along the lower branch of the slow manifold until reaching the LK and rapidly moving to less negative values of V. A regular burst will occur when the h_{NaP}-coordinate of the LK is less than the HB, and the V-coordinate of the lower bound of the periodic orbit is greater than that of
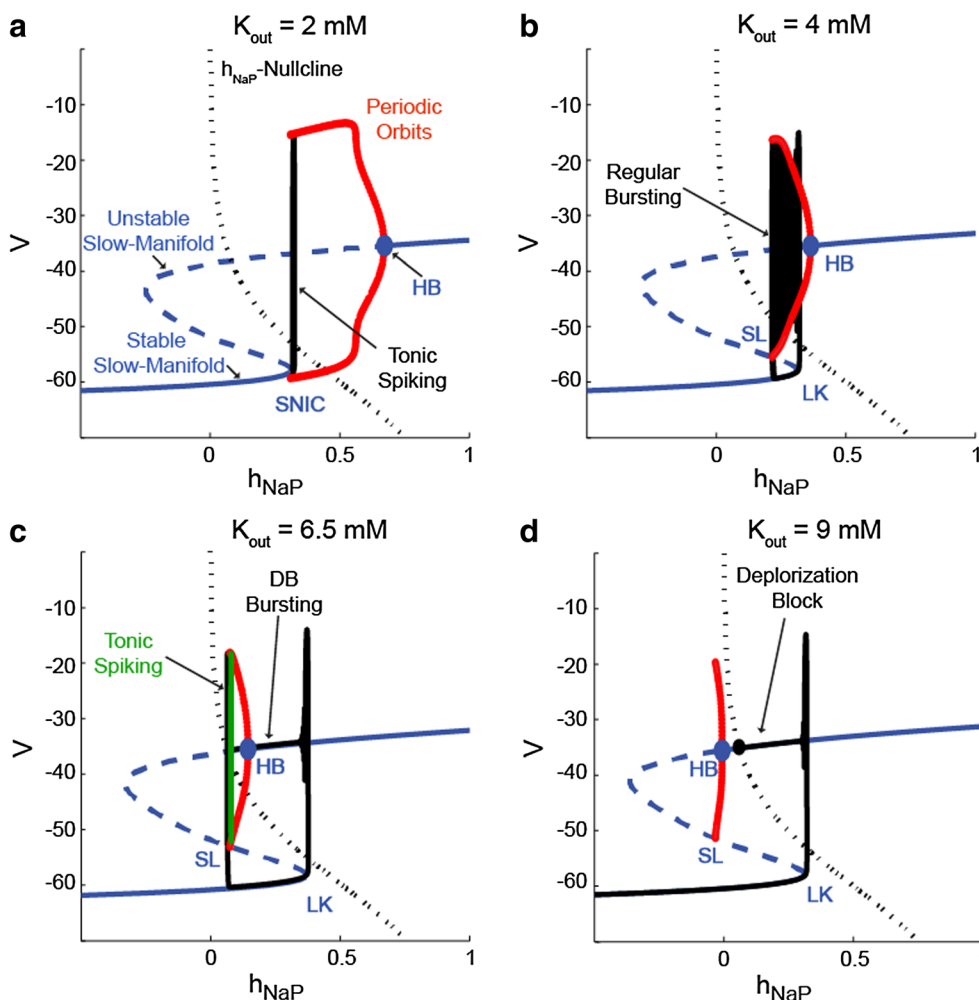
Fig. 3 Fast-slow analysis of transitions between tonic, bursting, and depolarization blocks at $drive = 0.32$, $\delta = 0$, and varying K_{out} (2 (**a**), 4 (**b**), 6.5 (**c**), and 9 mM (**d**)). The slow-manifold is depicted by *solid* and *dashed blue lines* when the critical points are stable and unstable, respectively. The lower and middle branches of the slow-manifold converge to result in a saddle node bifurcation, forming the lower knee of the slow-manifold (LK). When the slow-manifold loses its stability, at the *solid blue circle* representing the location of the Hopf bifurcation (HB), a periodic orbit emerges and its minimal and maximal V-coordinates are depicted with *red lines*. The h_{NaP}-nullcline is represented by a *dashed black line*. The *solid black line* represents the

neuron's trajectory in (h_{NaP}, V). **a** When the V-coordinate of the periodic orbit's lower boundary is less than the LK, a saddle node on an invariant circle (SNIC) bifurcation emerges. **b** Elevated K_{out} shifts the HB to lower h_{NaP}-coordinates, moving the periodic orbit to higher V-coordinates than the LK. This shift underlies the transition from a SNIC to a saddle loop (SL), or homoclinic, bifurcation scenario. **c** Bistable behavior when $K_{out} = 6.5$ mM. The initial conditions determine if tonic spiking (*green*) or DB bursting (*black*) occurs. **d** The trajectory reaches a stable state created by the intersection of the stable slow-manifold and the h_{NaP}-nullcline, depicted with a *solid black circle*

the LK (see Fig. 3b), this enables the neuron to activate and immediately assume periodic or bursting behavior. DB bursts occur when the opposite is true, i.e. the LK exists at higher values of h_{NaP} than the HB. This creates a trajectory where the burst initiates and oscillates down to the stable upper branch of the slow-manifold before resuming its oscillatory activity after the HB and ultimately terminating upon crossing the h_{NaP}-nullcline (see Fig. 3c).

All fast-slow decomposition diagrams were constructed in Matlab. Simulations were performed using XPPAUT (Ermentrout 2002).

3 Results

3.1 Effect of delayed rectifier potassium current on bursting patterns

Previous studies dealt with the depolarizing change to the leakage current from changing K_{out} and tended to neglect the effect of K_{out} on I_K current. We studied conditions when $\delta = 0$ to allow us to determine the impact of K_{out} on I_K with no effect upon the leakage current. This particular experiment allowed us to obtain a better understanding of the changes in the I_K current, in a manner not previously studied.

When $\delta = 0$, there are three main bursting regions (Fig. 2d). One-dimensional bifurcation diagrams were constructed to depict the single interspike interval of tonic spiking (Fig. 2a), as well as to differentiate between regular bursting (Fig. 2b), DB bursting, and the bistable regime of DB bursting and tonic spiking (Fig. 2c). The DB bursting had a period of depolarization without oscillations (Fig. 2c) and had two distinct clusters of large interspike intervals, i.e. intraburst and interburst intervals on the order of 1 and 10 s, respectively. We were able to distinguish regular and DB bursting by the presence of the intraburst interval branch on the one-dimensional bifurcation diagram (Fig. 2c). Figure 2d showed that DB bursting occurred with $\delta = 0$, when K_{out} was 4.5 to 7.0 mM. This finding was unexpected since experimental models typically demonstrate regular rather than DB bursting at high K_{out}. High K_{out} values caused I_K to be weaker because of increases in the potassium reversal potential, E_K, see Eqs. (4) and (18). Figure 2c shows an area of bistability of DB bursting and tonic spiking. The activation curve, which is the line at which quiescence transitions to active regimes, was vertical when $\delta = 0$ (Fig. 2d), thus there was no bursting for *drive* values less than ~0.3.

Fast-slow analysis of the regimes shown in Fig. 2 was performed for varying levels of K_{out} (Fig. 3). The slow-manifold (blue lines) has stable (solid blue) and unstable (dashed blue) portions. When K_{out} is low, i.e. 2 mM, the minimal V value on the periodic orbit (red lines) emerging from the Hopf bifurcation (HB), in the fast subsystem, extends to values of V below the lower knee (LK) of the slow-manifold creating the saddle-node loop, otherwise referred to as a saddle-node on invariant circle (SNIC) bifurcation (Fig. 3a). For a fixed value of h_{NaP} less than the h_{NaP}-coordinate of the LK, the lower branch of the slow-manifold is stable and the middle branch is unstable creating a system of a node and a saddle that move towards each other as h_{NaP} increases. When the image point reaches the LK of the slow-manifold, the stable node and saddle in the fast subsystem annihilate and the periodic orbit emerges. In the full system entering this orbit makes the voltage exhibit periodic (tonic) spiking. It is worth mentioning that in case of a SNIC bifurcation observed at low values of K_{out}, no bistability is present in the fast subsystem and hence no bursting is possible in the full system.

Fast-slow decomposition of the system when $K_{out} = 4$ mM shows that, in the fast subsystem, the stable quiescent state also disappears at the h_{NaP}-coordinate of the LK of the slow-manifold as h_{NaP} increases (Fig. 3b). However, the periodic orbits emerging from the HB terminate at a saddle-loop (SL) bifurcation (homoclinic bifurcation) where the limit cycle merges to the unstable (saddle) branch of the slow-manifold. Since this bifurcation happens at a lower h_{NaP}-coordinate than the LK of the slow-manifold, the fast subsystem is bistable between SL and LK thus creating prerequisites for bursting behavior.

Regular bursting occurs at K_{out} of 4 mM because the position of the HB is at a higher h_{NaP}-coordinate than the LK of the slow-manifold. Increasing K_{out} further, and thus reducing the h_{NaP}-coordinate of the HB, creates the prerequisites for DB bursting (Fig. 3c, black trajectory, see corresponding membrane potential trace Fig. 1c). When the system's trajectory reaches the LK of the slow-manifold it makes an upward jump towards the stable upper branch of the slow manifold and oscillates down to rest on this branch. However, the trajectory continues its leftward movement, due to the positioning of the h_{NaP}-nullcline, until it reaches the HB where the upper branch of the slow-manifold loses its stability. This loss of stability manifests as a reemergence of oscillatory activity contained by the limit cycle. However, this instability is extremely weak, so that the trajectory remains close to the high potential branch of the slow-manifold. When the trajectory eventually escapes the vicinity of the upper branch and reaches h_{NaP}-coordinates less than that of the SL, it falls to the stable low potential branch of the slow-manifold of the fast subsystem, indicating the neuron's return to a quiescent state in the fast subsystem.

This regime of DB bursting occurs, at $K_{out} = 6.5$ mM, when the system's initial conditions are outside the basin of attraction of the co-existing periodic orbit representing tonic spiking. The two regimes depicted in Fig. 3c correspond to the bistability shown in Fig. 2c, when *drive* = [0.3, 0.34].

Finally, when K_{out} is increased further, the h_{NaP}-nullcline intersects the upper branch of the slow-manifold at h_{NaP}-coordinates greater than the HB (Fig. 3e). This intersection creates a stable fixed point in the full system as it belongs to the stable high potential branch of the slow-manifold, and underlies the state of depolarization block (see membrane potential trace in Fig. 3d).

3.2 Bursting patterns when K_{out} affects the leakage current

When δ is positive (Fig. 4), K^+-ions contribute to I_L. Comparing the subpanels in Fig. 4, it is evident that δ has only a minor effect on the position of active regimes relative to K_{out} concentration. Note that in all subpanels of Fig. 4, K_{out} values of 2.0, 4.0, and 6.5 mM correspond to regimes of silence, regular bursting, and a co-existence of DB bursting and tonic activity, respectively. This happens for various magnitudes of δ though the *drive* values where these behaviors occur are shifted. In addition, the one-dimensional bifurcation diagrams at various δ values (not shown) indicated that the bursting patterns were strongly dependent on K_{out} levels. Increasing K_{out} caused a change from regular to DB bursting. In addition, as δ increased, the slope of the activation curve decreased. This change is caused by the stronger K^+-related leakage current, specifically, an increase in g_{LK} as seen in Eq. (23), which allowed small changes in K_{out} to have a more significant depolarizing effect. Therefore, the *drive* necessary to activate
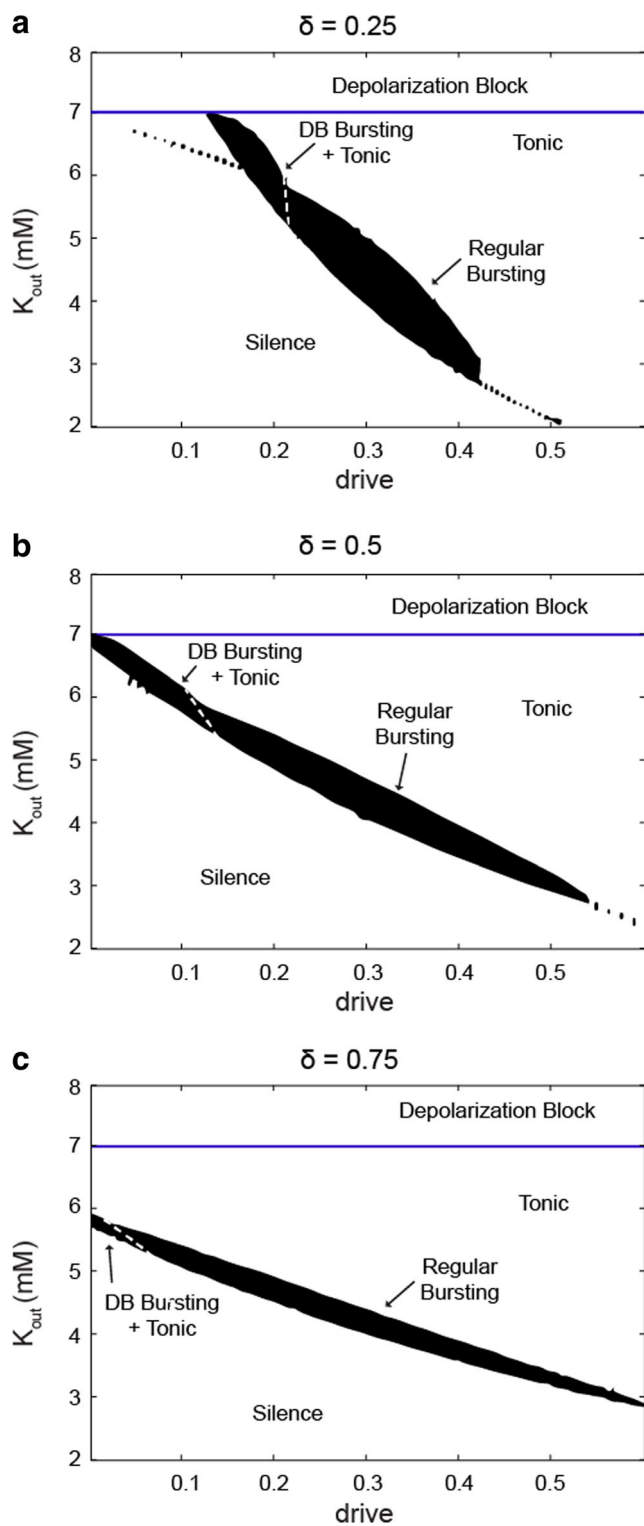
Fig. 4 Bifurcation diagrams with varying δ. Two-dimensional bifurcation diagrams with δ of 0.25 (**a**), 0.50 (**b**), 0.75 (**c**) showing neuronal regimes as K_{out} and *drive* were varied. The portion of bursting left of the *dashed white lines* represent areas of a bistability between DB bursting and tonic spiking, and areas to the right correspond to regular bursting. Depolarization block occurs at K_{out} values above the *blue line*. (**a**) In comparison to Fig. 2d ($\delta = 0$), the activation curve is no longer vertical, but similar changes in neuronal regimes were seen as K_{out} increased. (**b**, **c**). Increasing δ caused DB bursting to occur with *drive* = 0 and the activation curve became more horizontal. The range of K_{out} concentration defining the border between DB and regular bursting remained consistent with (**a**) and Fig. 2d

the neuron due to the depolarizing contribution of K_{out} to the leakage current when δ is greater than zero. The K_{out}-dependent decrease in the h_{NaP}-coordinate of the LK, becomes more dramatic as δ increases (see Fig. 5), but the h_{NaP}-coordinate of the HB does not demonstrate this same K_{out}-dependence. This implies that changes in the h_{NaP}-coordinate of the HB do not reflect the increased excitability caused by elevated K_{out}. Instead, movement of the HB is representative of I_K suppression, by an increased E_K.

When δ is 0.25 and *drive* is 0.35 the transition from silence to bursting, and later to tonic, is caused by a combination of these two movements (Fig. 6a–c). Silence occurs when the low potential branch of the slow-manifold intersects the h_{NaP}-nullcline, creating a stable fixed point where the trajectory converges (Fig. 6a, black solid black circle). Increasing K_{out} moves the LK to lower h_{NaP}-coordinates and when the h_{NaP}-nullcline no longer intersects the low potential branch of the slow-manifold, silence transitions to regular bursting (Fig. 6b). DB bursting occurs at slightly higher values of K_{out} (not shown) which causes a decrease in the h_{NaP}-coordinate of the HB, allowing the DB burst dynamics, described in Section 3.1, to emerge..

When K_{out} is increased to 6 mM the LK, and subsequently the SL, move to lower h_{NaP}-coordinates in the (h_{NaP}, V) plane (Fig. 6c). This pushes a substantial portion of the periodic orbit below the h_{NaP}-nullcline, where h_{NaP} has positive rate of change, thus preventing the neuron's trajectory from reaching the SL, and burst termination does not occur and tonic spiking persists (Fig. 6c). Finally, increasing K_{out} to 9 mM moves the HB to a lower h_{NaP}-coordinate than the one of the intersection of the h_{NaP}-nullcline and the upper branch of the slow-manifold (Fig. 6d). Because this intersection occurs at a point where the slow-manifold is stable, a new fixed point is created, and the neuron's trajectory terminates at this point (Fig. 6d, black circle). A stable fixed point on the upper branch of the slow-manifold is characteristic of a depolarization block. The exact relationship between the locations of these features, and their ability to produce regular or DB bursts was discussed previously in Section 3.1.

These results suggest that changes in K_{out} must impart an effect on I_L, i.e. $\delta > 0$, for the experimentally observed transitions between silence, bursting, and tonic spiking to occur

the neuron is progressively reduced for K_{out} concentrations above 4 mM.

Figure 5 shows that increasing K_{out} for non-zero values of δ causes a decrease in the h_{NaP}-coordinates of the Hopf bifurcation (HB) and the lower knee (LK) of the slow-manifold in the (h_{NaP}, V). The latter reflects an increase in the excitability of

Fig. 5 Movement of the Hopf bifurcation (HB) and lower knee (LK) of slow-manifold, to lower h_{NaP}-coordinates, when K_{out} is increased and *drive* = 0.35. All coloring is consistent with Fig. 3. Fast-slow analysis for $\delta = 0.25$ (**a**) and $\delta = 0.75$ (**b**) Larger δ results in a greater shift of the LK but not HB as K_{out} increases
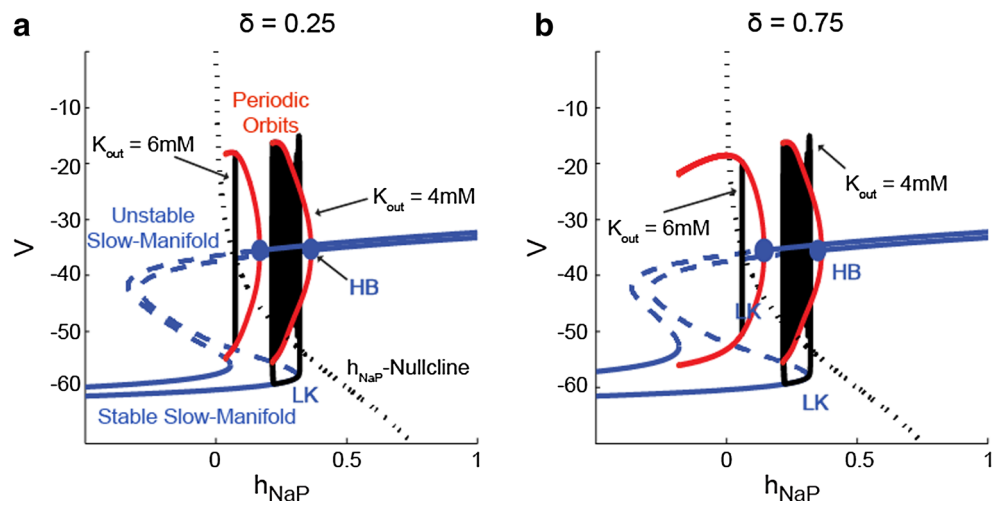

when K_{out} is increased (compare Figs. 4 and 3d). Moreover, the transitions between these behaviors are affected, and the regimes of DB bursting and depolarization block are created, by a decrease in the h_{NaP}-coordinate of a Hopf bifurcation in the fast subsystem when I_K is suppressed by an elevated K_{out}.

3.3 Bursting patterns without synaptic drive

Many experimental models use a cocktail of compounds, e.g. tetrodotoxin, curare, strychnine, etc., to block synaptic interactions between neurons. This is of particular interest when

Fig. 6 Fast-slow analysis of transitions between silence (**a**), bursting (**b**), tonic (**c**), and depolarization block (**d**) for $\delta = 0.25$, *drive* = 0.35, and varying levels of K_{out}. Coloring is consistent with Fig. 3. Stable equilibria of the fast subsystem, i.e. silence (**a**) and depolarization block (**d**), are depicted with *solid black circles*. K_{out} is 2, 4, 6, and 9 mM in sequential panels. Increasing K_{out} causes a leftward movement of both the Hopf bifurcation and the lower left knee of the slow-manifold when $\delta > 0$
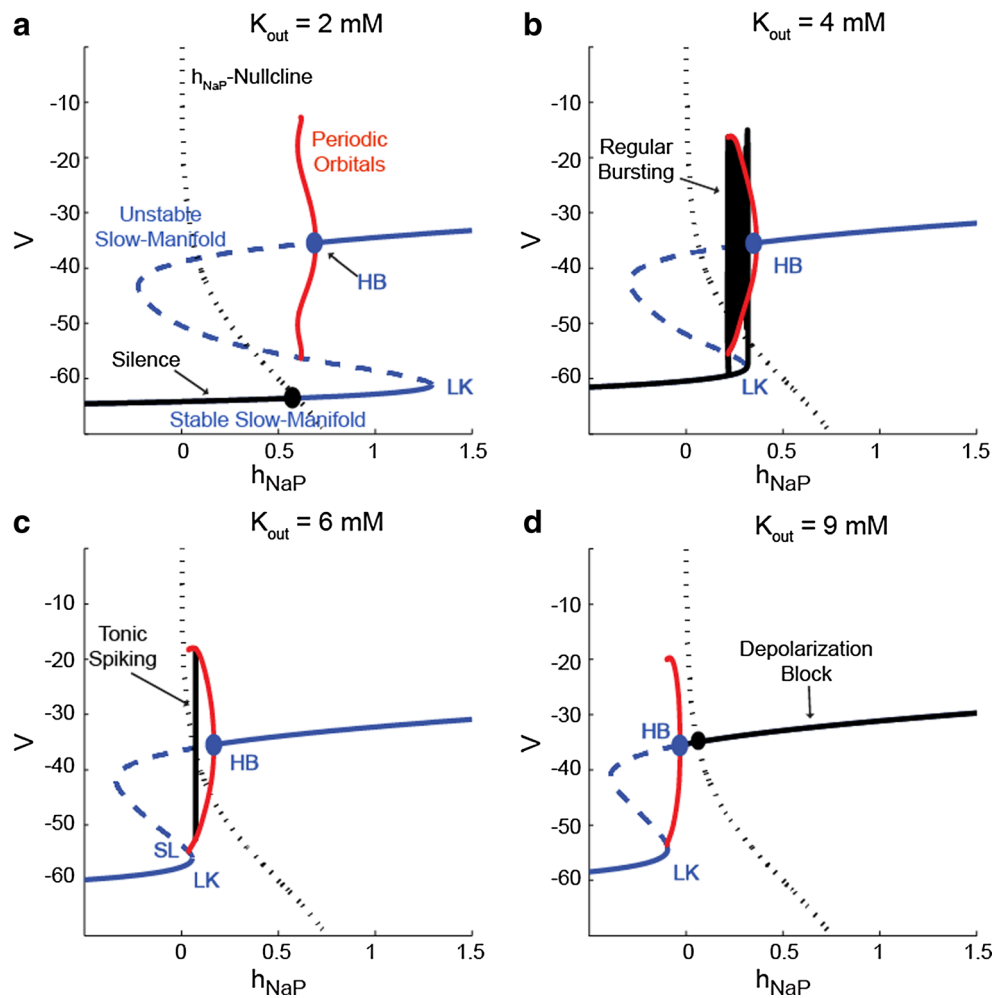
exploring the endogenous bursting capabilities of neurons (see Introduction). In our model, this experimental perturbation can be approximated by setting the conductance of the synaptic current, i.e. *drive*, to zero. Figure 7 shows a two-dimensional bifurcation diagram when *drive* = 0. Unlike the experimental results, see Johnson et al. 1994; Shao and Feldman 1997; Del Negro et al. 2001; Thoby-Brisson and Ramirez 2001, no regular bursting was observed. Instead only DB bursting occurred for all values of δ and K_{out}. Even when K_{out} was greater than 7 mM, bursting did not occur, only tonic spiking and depolarization block were observed.

3.4 Conductance of delayed rectifier potassium current (g_K)

Our model did not produce regular bursting at K_{out} concentrations that would be used to induce bursting *in vitro* (see Figs. 2d, 4 and 7), because of the attenuation of I_K. To counteract this we increased the current's maximal conductance, . $\overline{g}_K$, thus strengthening I_K, see Eq. (4). A stronger I_K, promotes repolarization, allowing the neuron to recover from depolarization block. Therefore, the advantage of $\overline{g}_K$ manipulation, as opposed to using K_{out}, is the ability to modulate only the delayed rectifier potassium current and not all currents that rely on a potassium gradient, i.e. the leakage current. The need for this form of specific modulation has been demonstrated in studies aimed at preventing hypoxia induced apoptosis by down-regulating only the delayed rectifier potassium current (Yu et al. 1997; Wei et al. 2003). Additionally, down regulation of $\overline{g}_K$ to suppress I_K, and induce bursting in a quiescent neuron, suggested that bursting may be induced without the general increase in excitability thought responsible for bursting when K_{out} is increased. We investigated this by evaluating
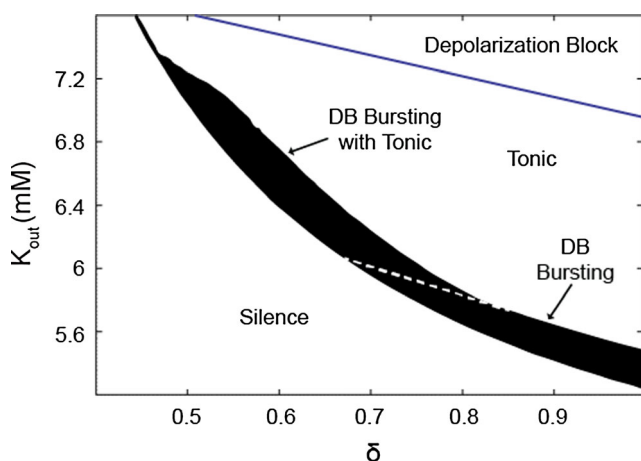

Fig. 7 Two-dimensional bifurcation diagram of K_{out} vs. δ. The *dashed white line* separates DB bursting (*below line*) and a bistable region of DB bursting and tonic spiking. Above the *solid blue line* depolarization block occurs. Boundaries were calculated by creating one-dimensional bifurcation diagrams were K_{out} was varied at fixed values of δ

the neuronal regimes that occurred when $\overline{g}_K$ was varied at different K_{out} concentrations. To restrict the number of control parameters we set $\delta = 0$. Figures 8b and 9 show two-dimensional bifurcation diagrams on the (*drive*, $\overline{g}_K$) and (δ, $\overline{g}_K$) planes with K_{out} concentrations of 4 and 8 mM, respectively. We chose these values of K_{out} because 4 mM is a typically reported *in vivo* concentration (Hall 2010) and *in vitro* experiments often elevate extracellular potassium to 8 mM to induce bursting (Koshiya and Smith 1999).

With $K_{out} = 4$ mM, regular bursting occurred when $\overline{g}_K = [123, 217$ nS]. However, $\overline{g}_K$ values above 200 nS produced an atypical form of regular bursting, with only a few spikes comprising each burst (see Fig. 8a). When K_{out} was set to 8 mM, regular bursting only occurred when $\delta = [0.38, 0.454]$ and $\overline{g}_K = [225, 475]$ nS. The lack of overlap between the $\overline{g}_K$ ranges for regular bursting indicates that the bursting mechanisms in our model may be insufficient to explain behaviors observed at *in vivo* and *in vitro* concentration of extracellular potassium.

4 Discussion

The model proposed in this study was derived from the previous persistent sodium-based models of a pre-BötC (Butera et al. 1999a, b), where an external drive or change in the leakage reversal potential were used to evoke bursting. In contrast, *in vitro* studies induced bursting by elevating extracellular potassium (K_{out}). It has been proposed that elevation of K_{out} increases the reversal potential of the leakage current, and thus increases the neuronal excitability in a similar manner to changing *drive*. In our study, we directly simulated the effect of increasing K_{out} on the bursting patterns of the neuron, and investigated the interplay between the delayed rectifier potassium and leakage currents.

Fast-slow decomposition analysis revealed that bursting was the result of a transition from a saddle node on an invariant circle (SNIC) bifurcation to a saddle-loop (or homoclinic) bifurcation occurring in the fast subsystem. Specifically, when the delayed rectifier potassium current, I_K, was suppressed by increasing K_{out}, or reducing $\overline{g}_K$, the *V*-range of the periodic orbit emanating from the Hopf bifurcation (HB) transitioned from enclosing the system of a stable node and saddle, and thus forming the SNIC bifurcation (see Fig. 3a), to existing at higher *V*-coordinates, in the (h_{NaP}, *V*) plane, than the stable node and saddle, thus forming a saddle-loop bifurcation (Figs. 3b). Moreover, the position of the HB relative to the lower knee (LK) of the slow-manifold, is of particular relevance when the LK is moved to lower h_{NaP}-coordinates by increasing the *drive* or K_{out} when $\delta > 0$. It was demonstrated in the previous sections that the transition from bursting to tonic spiking relied on a different qualitative mechanism than the transition from silence to bursting described above.
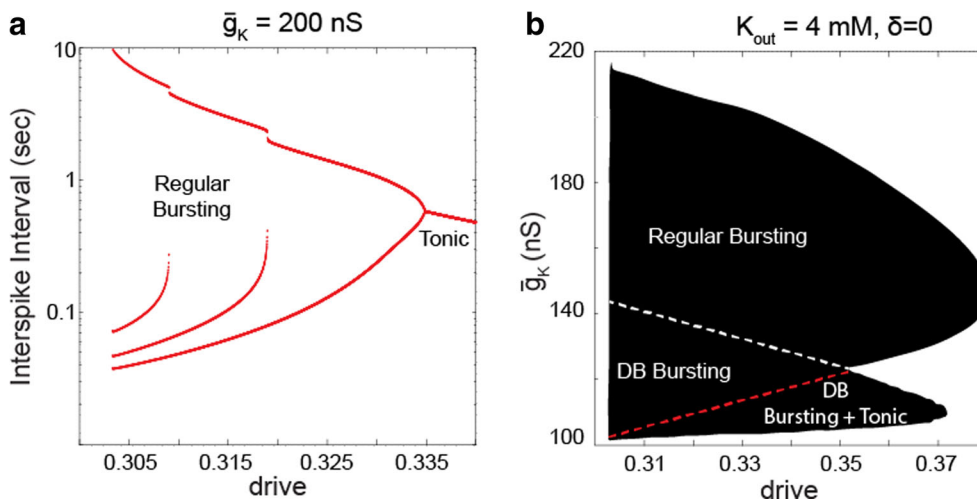
Fig. 8 Varying $\bar{g}_K$ with $K_{out} = 4$ mM and $\delta = 0$. **a** One-dimensional bifurcation diagram showed only regular bursting at $\bar{g}_K = 200$ nS, however, these bursts uncharacteristically contained three or fewer spikes per burst. **b** Two-dimensional bifurcation diagram showed that regular bursting occurred when $\bar{g}_K = [125, 210]$ nS, depending on the value of *drive* used. DB bursting occurred below the white dashed line, and the area above represents areas of regular bursting. The DB bursting area was further divided into just DB bursting (above the *red dashed line*) and an area of bistability between DB bursting and tonic spiking. Boundaries were calculated by creating one-dimensional bifurcation diagrams were $\bar{g}_K$ was varied for fixed values of *drive*

Specifically, a burst failed to terminate, and thus remained as tonic spiking, when the periodic orbit of the HB failed to reach the saddle loop (Fig. 3c, green trajectory). It was also shown that moving the HB to lower h_{NaP}-coordinates eventually led to a depolarization block. Lastly, when the upper branch of the slow-manifold intersected with the h_{NaP}-nullcline, creating a stable fixed point, the neuron's membrane potential remained at a constant, and depolarized, voltage.

In addition to the artificial increase in K_{out} used *in vitro*, fluctuations in I_K properties may occur naturally, and therefore
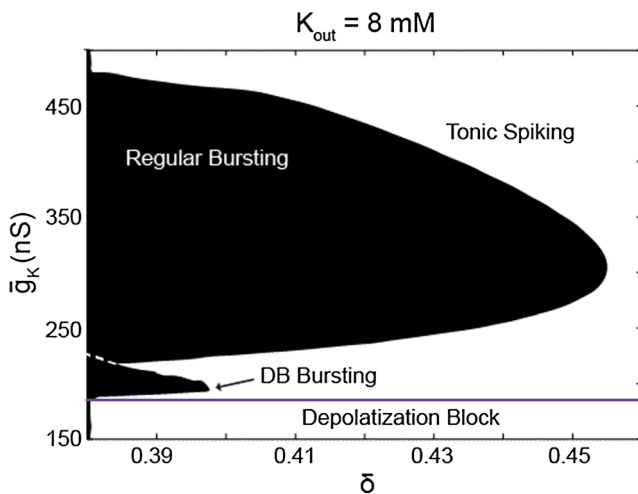

Fig. 9 Bifurcation diagram of $\bar{g}_K$ vs δ, when $K_{out} = 8$ mM. The portion of bursting below the *white dashed line* represents areas of DB bursting, and areas above represents areas of regular bursting. Below the *blue solid line* depolarization block occurs. Boundaries were calculated by creating one-dimensional bifurcation diagrams with varying values of $\bar{g}_K$ at a fixed value of δ

contribute to pathological behavior of the neurons. Hypoxic conditions disrupt the upward ramping phrenic nerve waveform, characteristic of eupneic breathing (Richter and Ballantyne 1983). Furthermore, hypoxic conditions cause periods of apnea and, depending on the magnitude and duration of oxygen deprivation, may cause gasping behavior. Gasping is characterized by a decrementing phrenic nerve activity during bursts and may arise from different regions of the medulla than those responsible for the eupneic rhythm (St-John 1990; St-John et al. 2002) or may be closely related to chemosensitive pacemaker cells in the pre-Bötzinger complex (Solomon et al. 2000). It has also been demonstrated, in *in vivo* studies, that hypoxia induced gasping correlates with a sharp rise in extracellular potassium concentrations (Melton et al. 1991, 1996). The rise in K_{out} is a direct result of the declining energy production caused by sustained hypoxia (Lipinski and Bingmann 1986; Morris 1974), but a direct causal relationship between rising K_{out} and gasping has yet to be established. In addition to the rise in K_{out}, hypoxia has been shown to suppress various voltage-gated potassium channels, though this is likely a secondary effect of elevated K_{out} (Jiang and Haddad 1994; Conforti and Millhorn 1997; Thompson and Nurse 1998; Gebhardt and Heinemann 1999; Liu et al. 1999; Lopez-Barneo et al. 2001). In addition to altered potassium dynamics, an augmentation of the persistent sodium current, I_{NaP}, has been observed during hypoxic conditions (Hammarstrom and Gage 1998, 2000, 2002; Kawai et al. 1999). It was shown that the effects of hypoxic conditions may be manipulated, independently, to produce rhythmic bursting in a computational model (Rybak et al. 2004a). This work has led some to hypothesize that the transition from eupnea to gasping is representative of a switch from a

network-based to endogenous bursting driven mechanism, respectively, and the sharp rise in K_{out} likely plays an important role in the transition (Rybak et al. 2002; St-John et al. 2002). The work in the present study seeks to elucidate the mechanisms through which endogenous bursting could be produced by such a rise in K_{out} in both *in vitro* and *in vivo* conditions.

The results of our simulations indicate that bursting was primarily the result of I_K suppression, and even though increases in neuronal excitability are necessary, they are not sufficient to induce and sustain bursting behavior. To supplement this argument, a two-dimensional bifurcation diagram was built to examine how the range of K_{out} values where bursting occurred changed as the potassium contribution to the leakage current (δ) increased (Fig. 10). This was performed at a fixed value of *drive* = 0.35, that was known to cause bursting based on prior simulations, see Figs. 2 and 4. When $\delta = 0$ the K_{out} concentration imparted no effect on network excitability, i.e. I_L, and operated strictly by suppressing I_K. However, as δ increased, so did I_L, but the impact on I_K remained constant. The resultant effect was a progressively smaller range of K_{out} values over which bursting was observed as δ increased. This result demonstrated that increased network excitability, via δ, and therefore I_L, diminished K_{out} induced bursting activity.

We introduce the concept of regular versus DB bursting in Section 3.1. The period of sustained depolarization within a DB burst corresponds to a cessation of neuronal activity that may contribute to abnormal respiratory rhythm. We separated the two types of bursting using one-dimensional bifurcation diagrams (Fig. 2b, c). The separation of bursting into these two types has not been previously investigated, and would benefit from more detailed analysis in the future. More rigid definitions could be created by extending the work presented in this paper. Exact boundaries could be calculated from the relative positions of the HB and the LK of slow-manifold in
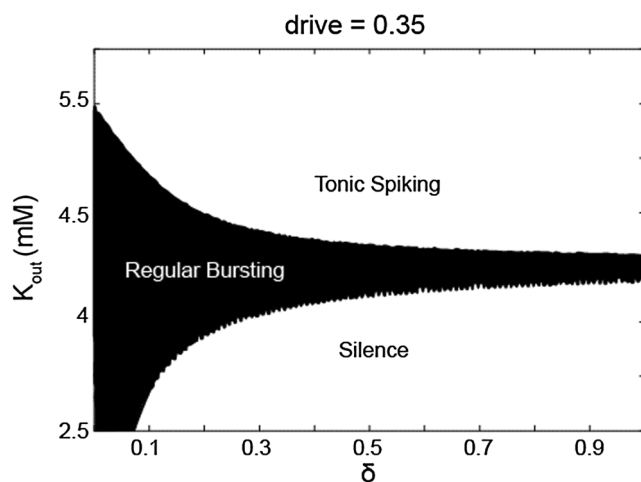
terms of their h_{NaP}-coordinates. Specifically, regular bursting occurred when the h_{NaP}-coordinate of the HB is greater than the LK, assuming all other parameters are such that bursting occurs. The transition point to DB bursting occurred when the HB and LK moved to a point where their h_{NaP}-coordinates were equal.

Changing δ did not have a substantial effect upon the position of bursting regimes with respect to different levels of K_{out}, see Fig. 4. Therefore, the use of any value of δ in theoretical models is acceptable for the study of bursting patterns at different K_{out} values. The greatest effect of changing δ was on the slope of the activation curve. As δ increased this curve became more horizontal (Fig. 4a–c) and intersected the *drive* = 0 line. This finding indicated that active regimes could exist in the absence of synaptic connections. However, our data shows that regular bursting did not occur when *drive* = 0 (Fig. 7), instead, only DB bursting was observed.

Neuronal regime transitions from silence to bursting, and then to tonic spiking has been demonstrated *in vitro* as K_{out} was progressively elevated (Del Negro et al. 2001). Additionally, bursting had a higher frequency as K_{out} increased. When K_{out} did not contribute to I_L, i.e. $\delta = 0$, increasing K_{out} never caused a transition to bursting (Fig. 2d). In this scenario the boundary between silence and active regimes was completely independent of K_{out}. However, when δ was increased (Fig. 4), we found that, with moderate values of *drive*, it was possible to transition directly from silence to regular bursting to tonic spiking, as seen on the bifurcation diagrams with δ of 0.25, 0.5, and 0.75 (Fig. 4). The frequency of bursting during these transitions also increased with K_{out} (not shown), as was reported experimentally (Del Negro et al. 2001).

The lack of bursting at K_{out} of 8 mM when *drive* = 0 (see Fig. 7) indicated that I_K may have been too weak, and therefore the neuron could not repolarize. We increased $\overline{g}_K$ to strengthen I_K and study its effect upon burst patterns (Fig. 9). We found that for bursting to occur at K_{out} = 8 mM and *drive* = 0, δ had to be in the range of 0.38 to 0.45. Bursting did not occur at higher values ($\delta > 0.45$). This finding contradicts the view that K^+ is the principal factor in the hyperpolarizing leakage current, as previously thought. Forsythe and Redman 1988 reported a ratio 0.25 for the conductance of the Cl^- and K^+ leakage components. This would correspond, in our model, to a δ of 0.8, significantly greater than our predicted values.

We found that regular bursting only occurred at $\overline{g}_K$ values below 217 nS, when K_{out} was 4 mM (Fig. 8), and above 225 nS when K_{out} was 8 mM (Fig. 9). Thus, regular bursting could not occur at the same value of $\overline{g}_K$ at K_{out} levels of 4 and 8 mM. This result suggests that the mechanisms commonly attributed to endogenous bursting in pre-BötC neurons *in vitro*, and used in our computational model, may be insufficient for burst production *in vivo*. Moreover when K_{out} was 4 mM, the

Fig. 10 Bifurcation diagram of K_{out} vs δ when *drive* = 0.35. As δ increases there is a noticeable decrease in the range of K_{out} values where bursting occurred

transition from quiescence to the only active regime, i.e. tonic spiking, occurred through a SNIC bifurcation. This suggests that, *in vivo*, neurons may demonstrate type I excitability, which in many cases allows for a substantially simplified description (Izhikevich 2000). Consequently, our results suggest that rhythmic activity *in vivo* is likely to rely on other mechanisms than can be accounted for with the commonly-accepted models. For example, Jasinski et al. 2013 showed that recurrent synaptic excitation, in combination with the sodium-potassium exchanger (pump), produced robust rhythmic network activity even when all intrinsic bursting mechanisms were blocked.

To test our modeling predictions, a current could be applied to a neuron at low concentration of K_{out}. This would be similar to artificial increase in the neuron's synaptic *drive*, and show whether bursting occurs at low K_{out} concentrations, such as those observed *in vivo*. Another possible *in vitro* study would be decreasing extracellular Cl^- concentration. This would enable manipulation of the leakage current without affecting the delayed rectifier potassium current. If we transition directly from silence to spiking it would further strengthen our claim that bursting cannot occur at low K_{out} concentrations.

The above collection of findings suggests that either the current experimental models do not correlate with the physiology *in vivo* and/or there are errors in the assumptions underlying current theoretical models. The use of the sodium-potassium pump suggested by Jasinski et al. 2013 may increase the area of bursting on a two-dimensional bifurcation diagram of *drive* versus K_{out}. Such an increase in the bursting area may help explain the mechanistic discrepancies, between *in vivo* and *in vitro* burst generation, highlighted by our work. Another potential issue with the theoretical model may relate to our exclusion of calcium-based currents. However, it should be noted that there is conflicting evidence regarding the importance of calcium-related channels in the activity of respiratory neurons (Del Negro et al. 2001; Rubin et al. 2009; Ramirez et al. 2011). In addition, we assumed that the potassium reversal potential followed the Nernst equation, but it has previously been suggested that there may be deviations from the Nernst equations for K_{out} concentrations less than 10 mM (Forsythe and Redman 1988).

In conclusion, the results of our study suggest that elevation of extracellular potassium concentration attenuates potassium currents. This effect underlies the emergence of the endogenous bursting observed in individual neurons of the pre-BötC, which is putatively sustained by the slowly inactivating persistent sodium current. However, physiologic concentrations of extracellular potassium may be insufficient for suppression of these currents and the development of endogenous bursting. Our modeling study suggests that neuronal bursting *in vivo* is unlikely to be endogenous and instead may result from network interactions.

References

Butera, R. J., Rinzel, J., & Smith, J. C. (1999a). Models of respiratory rhythm generation in the pre-Botzinger complex. I. Bursting pacemaker neurons. *Journal of Neurophysiology, 82*, 382–397.

Butera, R. J., Rinzel, J., & Smith, J. C. (1999b). Models of respiratory rhythm generation in the pre-Botzinger complex. II. Populations of coupled pacemaker neurons. *Journal of Neurophysiology, 82*, 398–415.

Conforti, L., & Millhorn, D. E. (1997). Selective inhibition of a slow-inactivating voltage-dependent K+ channel in rat PC12 cells by hypoxia. *The Journal of Physiology, 502*(Pt 2), 293–305.

Del Negro, C. A., Johnson, S. M., Butera, R. J., & Smith, J. C. (2001). Models of respiratory rhythm generation in the pre-Botzinger complex. III. Experimental tests of model predictions. *Journal of Neurophysiology, 86*, 59–74.

Ermentrout, B. (2002). *Simulating, analyzing, and animating dynamical systems : A guide to XPPAUT for researchers and students*. Philadelphia: SIAM.

Forsythe, I. D., & Redman, S. J. (1988). The dependence of motoneurone membrane potential on extracellular ion concentrations studied in isolated rat spinal cord. *The Journal of Physiology, 404*, 83–99.

Gebhardt, C., & Heinemann, U. (1999). Anoxic decrease in potassium outward currents of hippocampal cultured neurons in absence and presence of dithionite. *Brain Research, 837*, 270–276.

Guttman, R., Lewis, S., & Rinzel, J. (1980). Control of repetitive firing in squid axon membrane as a model for a neuroneoscillator. *The Journal of Physiology, 305*, 377–395.

Hall, J. E. (2010). Elsevier: Guyton and Hall Textbook of Medical Physiology, 12th Edition (Thirteenth).

Hammarstrom, A. K., & Gage, P. W. (1998). Inhibition of oxidative metabolism increases persistent sodium current in rat CA1 hippocampal neurons. *The Journal of Physiology, 510*(Pt 3), 735–741.

Hammarstrom, A. K., & Gage, P. W. (2000). Oxygen-sensing persistent sodium channels in rat hippocampus. *The Journal of Physiology, 529*(Pt 1), 107–118.

Hammarstrom, A. K., & Gage, P. W. (2002). Hypoxia and persistent sodium current. *European Biophysics Journal, 31*, 323–330.

Huguenard, J. R., & McCormick, D. A. (1992). Simulation of the currents involved in rhythmic oscillations in thalamic relay neurons. *Journal of Neurophysiology, 68*(4), 1373–1383.

Izhikevich, E. M. (2000). Neural excitability, spiking and bursting. *International Journal of Bifurcation and Chaos, 10*(06), 1171–1266.

Jasinski, P. E., Molkov, Y. I., Shevtsova, N. A., Smith, J. C., & Rybak, I. A. (2013). Sodium and calcium mechanisms of rhythmic bursting in excitatory neural networks of the pre-Botzinger complex: a computational modelling study. *The European Journal of Neuroscience, 37*, 212–230.

Jiang, C., & Haddad, G. G. (1994). A direct mechanism for sensing low oxygen levels by central neurons. *Proceedings of the National Academy of Sciences of the United States of America, 91*, 7198–7201.

Johnson, S. M., Smith, J. C., Funk, G. D., & Feldman, J. L. (1994). Pacemaker behavior of respiratory neurons in medullary slices from neonatal rat. *Journal of Neurophysiology, 72*, 2598–2608.

Kantz, H., & Schreiber, T. (2004). *Nonlinear time series analysis*. Cambridge: Cambridge University Press.

Kawai, Y., Qi, J., Comer, A. M., Gibbons, H., Win, J., & Lipski, J. (1999). Effects of cyanide and hypoxia on membrane currents in neurones acutely dissociated from the rostral ventrolateral medulla of the rat. *Brain Research, 830*, 246–257.

Koizumi, H., & Smith, J. C. (2008). Persistent Na + and K + −dominated leak currents contribute to respiratory rhythm generation in the pre-Botzinger complex in vitro. *Journal of Neuroscience, 28*, 1773–1785.

Koshiya, N., & Smith, J. C. (1999). Neuronal pacemaker for breathing visualized in vitro. *Nature, 400*(6742), 360–363.

Lawson, E. E., Richter, D. W., & Bischoff, A. (1989). Intracellular recordings of respiratory neurons in the lateral medulla of piglets. *Journal of applied physiology (Bethesda, Md.: 1985), 66*(2), 983–8.

Lipinski, H. G., & Bingmann, D. (1986). pO2-dependent distribution of potassium in hippocampal slices of the guinea pig. *Brain research, 380*(2), 267–75.

Liu, H., Moczydlowski, E., & Haddad, G. G. (1999). O(2) deprivation inhibits Ca(2+)-activated K(+) channels via cytosolic factors in mice neocortical neurons. *The Journal of Clinical Investigation, 104*, 577–588.

Lopez-Barneo, J., Pardal, R., & Ortega-Saenz, P. (2001). Cellular mechanism of oxygen sensing. *Annual Review of Physiology, 63*, 259–287.

Melton, J. E., Chae, L. O., Neubauer, J. a, & Edelman, N. H. (1991). Extracellular potassium homeostasis in the cat medulla during progressive brain hypoxia. *Journal of applied physiology (Bethesda, Md.: 1985), 70*(4), 1477–1482.

Melton, J. E., Kadia, S. C., Yu, Q. P., Neubauer, J. A, & Edelman, N. H. (1996). Respiratory and sympathetic activity during recovery from hypoxic depression and gasping in cats. *Journal of applied physiology (Bethesda, Md.: 1985), 80*(6), 1940–1948.

Molkov, Y. I., Abdala, A. P., Bacak, B. J., Smith, J. C., Paton, J. F. R., & Rybak, I. A. (2010). Late-expiratory activity: emergence and interactions with the respiratory CpG. *Journal of neurophysiology, 104*(5), 2713–29.

Morris, M. E. (1974). Hypoxia and extracellular potassium activity in the guinea-pig cortex. *Canadian journal of physiology and pharmacology, 52*(4), 872–82.

Ramirez, J., Zuperku, E. J., Alheid, G. F., Lieske, S. P., Ptak, K., & Mccrimmon, D. R. (2002). Respiratory rhythm generation: converging concepts from in vitro and in vivo approaches? *Respiratory physiology & neurobiology, 131*(1-2), 43–56.

Ramirez, J. M., Koch, H., Garcia, A. J., Doi, A., & Zanella, S. (2011). The role of spiking and bursting pacemakers in the neuronal control of breathing. *Journal of Biological Physics, 37*, 241–261.

Richter, D. W. (1982). Generation and maintenance of the respiratory rhythm. *The Journal of experimental biology, 100*, 93–107.

Richter, D., & Ballantyne, D. (1983). Central Neurone Environment and the Control Systems of Breathing and Circulation. In M. E. Schläfke, W. R. See, & H.-P. Koepchen, (Eds.). Berlin, Heidelberg: Springer. doi:10.1007/978-3-642-68657-3

Richter, D., & Spyer, K. M. (2001). Studying rhythmogenesis of breathing: Comparison of in vivo and in vitro models. *Trends in Neurosciences, 24*(8), 464–72.

Richter, D., & Smith, J. C. (2014). Respiratory rhythm generation in vivo. Physiology (Bethesda, Md.), 29(1), 58–71.

Rinzel, J. (1985). Excitation dynamics: insights from simplified membrane models. *Federation Proceedings, 44*, 2944–2946.

Rubin, J. E., Hayes, J. A., Mendenhall, J. L., & Del Negro, C. A. (2009). Calcium-activated nonspecific cation current and synaptic depression promote network-dependent burst oscillations. *Proceedings of the National Academy of Sciences of the United States of America, 106*, 2939–2944.

Rybak, I. A., Paton, J. F. R., Rogers, R. F., & St-John, W. M. (2002). Generation of the respiratory rhythm: State-dependency and switching. *Neurocomputing, 44-46*, 605–614. doi:10.1016/S0925-2312(02)00447-2.

Rybak, I. A., Ptak, K., Shevtsova, N. A., & McCrimmon, D. R. (2003a). Sodium currents in neurons from the rostroventrolateral medulla of the rat. *Journal of Neurophysiology, 90*, 1635–1642.

Rybak, I. A., Shevtsova, N. A., St-John, W. M., Paton, J. F. R., & Pierrefiche, O. (2003b). Endogenous rhythm generation in the pre-Botzinger complex and ionic currents: modelling and in vitro studies. *European Journal of Neuroscience, 18*, 239–257.

Rybak, I. A., Shevtsova, N. A., Ptak, K., & McCrimmon, D. R. (2004a). Intrinsic bursting activity in the pre-Botzinger Complex: role of persistent sodium and potassium currents. *Biological Cybernetics, 90*, 59–74.

Rybak, I. A., Shevtsova, N. A., Paton, J. F. R., Dick, T. E., St-John, W. M., Mörschel, M., & Dutschmann, M. (2004b). Modeling the pontomedullary respiratory network. *Respiratory Physiology and Neurobiology, 143*(2-3), 307–19.

Rybak, I. A., Shevtsova, N. A., Paton, J. F. R., Pierrefiche, O., St-John, W. M., & Haji, A. (2004c). Modelling respiratory rhythmogenesis: focus on phase switching mechanisms. *Advances in experimental medicine and biology, 551*, 189–194.

Rybak, I. A., Abdala, A. P., Markin, S., Paton, J. F. R., & Smith, J. C. (2007). Spatial organization and state-dependent mechanisms for respiratory rhythm and pattern generation. *Progress in brain research, 165*, 201–20.

Shao, X. M., & Feldman, J. L. (1997). Respiratory rhythm generation and synaptic inhibition of expiratory neurons in pre-Botzinger complex: differential roles of glycinergic and GABAergic neural transmission. *Journal of Neurophysiology, 77*, 1853–1860.

Smith, J. C., Ellenberger, H. H., Ballanyi, K., Richter, D. W., & Feldman, J. L. (1991). Pre-Botzinger Complex - a brain-stem region that may generate respiratory rhythm in mammals. *Science, 254*, 726–729.

Smith, J. C., Butera, R. J., Koshiya, N., Del Negro, C., Wilson, C. G., & Johnson, S. M. (2000). Respiratory rhythm generation in neonatal and adult mammals: The hybrid pacemaker-network model. *Respiration Physiology, 122*(2-3), 131–147.

Smith, J. C., Abdala, A. P., Koizumi, H., Rybak, I. A., & Paton, J. F. R. (2007). Spatial and functional architecture of the mammalian brain stem respiratory network: a hierarchy of three oscillatory mechanisms. *Journal of neurophysiology, 98*(6), 3370–87.

Smith, J. C., Abdala, A. P., Rybak, I. A., & Paton, J. F. R. (2009). Structural and functional architecture of respiratory networks in the mammalian brainstem. Philosophical transactions of the Royal Society of London. *Series B, Biological sciences, 364*(1529), 2577–87.

Smith, J. C., Abdala, A. P., Borgmann, A., Rybak, I. A., & Paton, J. F. (2013). Brainstem respiratory networks: building blocks and microcircuits. *Trends in Neurosciences, 36*, 152–162.

Solomon, I. C., Edelman, N. H., & Neubauer, J. A. (2000). Pre-Bötzinger complex functions as a central hypoxia chemosensor for respiration in vivo. *Journal of neurophysiology, 83*(5), 2854–68.

St-John, W. M. (1990). Neurogenesis, control, and functional significance of gasping. *Journal of Applied Physiology, 68*(4), 1305–1315.

St-John, W. M., Rybak, I. A., & Paton, J. F. R. (2002). Potential switch from eupnea to fictive gasping after blockade of glycine transmission and potassium channels. *American journal of physiology. Regulatory, integrative and comparative physiology, 283*(3), R721–R731.

Thoby-Brisson, M., & Ramirez, J. M. (2001). Identification of two types of inspiratory pacemaker neurons in the isolated respiratory neural network of mice. *Journal of Neurophysiology, 86*, 104–112.

Thompson, R. J., & Nurse, C. A. (1998). Anoxia differentially modulates multiple K+ currents and depolarizes neonatal rat adrenal chromaffin cells. *The Journal of Physiology, 512*(Pt 2), 421–434.

Wei, L., Yu, S. P., Gottron, F., Snider, B. J., Zipfel, G. J., & Choi, D. W. (2003). Potassium channel blockers attenuate hypoxia- and ischemia-induced neuronal death in vitro and in vivo. *Stroke; A Journal of Cerebral Circulation, 34*, 1281–1286.

Yu, S. P., Yeh, C. H., Sensi, S. L., Gwag, B. J., Canzoniero, L. M., Farhangrazi, Z. S., Ying, H. S., Tian, M., Dugan, L. L., & Choi, D. W. (1997). Mediation of neuronal apoptosis by enhancement of outward potassium current. *Science, 278*, 114–117.